

Power grid stability under perturbation of single nodes: Effects of heterogeneity and internal nodes

Matthias Wolff, Pedro G. Lind and Philipp Maass

Fachbereich Physik, Universität Osnabrück, Barbarastrasse 7, 49076 Osnabrück, Germany

E-mail: mawolff@uos.de, pelind@uos.de, maass@uos.de

Abstract. Non-linear equations describing the time evolution of frequencies and voltages in power grids exhibit fixed points of stable grid operation. The dynamical behaviour after perturbations around these fixed points can be used to characterise the stability of the grid. We investigate both probabilities of return to a fixed point and times needed for this return after perturbation of single nodes. Our analysis is based on an IEEE test grid and the second-order swing equations for voltage phase angles θ_j at nodes j in the synchronous machine model. The perturbations cover all possible changes $\Delta\theta$ of voltage angles and a wide range of frequency deviations in a range $\Delta f = \pm 1$ Hz around the common frequency $\omega = 2\pi f = \dot{\theta}_j$ in a synchronous fixed point state. Extensive numerical calculations are carried out to determine, for all node pairs (j, k) , the return times $t_{jk}(\Delta\theta, \Delta\omega)$ of node k after a perturbation of node j . We find that for strong perturbations of some nodes, the grid does not return to its synchronous state. If returning to the fixed point, the times needed for the return are strongly different for different disturbed nodes and can reach values up to 20 seconds and more. When homogenising transmission line and node properties, the grid always returns to a synchronous state for the considered perturbations, and the longest return times have a value of about 4 seconds for all nodes. The neglect of reactances between points of power generation (internal nodes) and injection (terminal nodes) leads to an underestimation of return probabilities.

1. Introduction

Due to the increasing share of renewable energy sources on power production, questions concerning the limits, quantification and control of power grid stability pose new challenges. These challenges can be taken on by a combination of methods developed in the fields of non-linear dynamics, network theory and stochastic modelling [1, 2, 3, 4, 5, 6, 7, 8]. Generally, for studying power grids, models are needed for the dynamics of voltages and frequencies as well as for the grid representation. However, it is still unclear, which detailedness of modelling is needed for a reliable quantification of grid stability.

For studying power grid dynamics, various approaches have been used in the literature [9], which essentially differ in the treatment of the coupling of generators and loads to the grid, and the treatment of the voltage dynamics. A widely used approach is the synchronous machine model, where the dynamics of both generators and loads are described by the swing equation for synchronous machines, and where the time-dependence of the moduli of their complex voltage amplitudes is considered to be negligible. Refined models with dynamics of voltage amplitude moduli were considered [3, 10] and recent results indicate that these

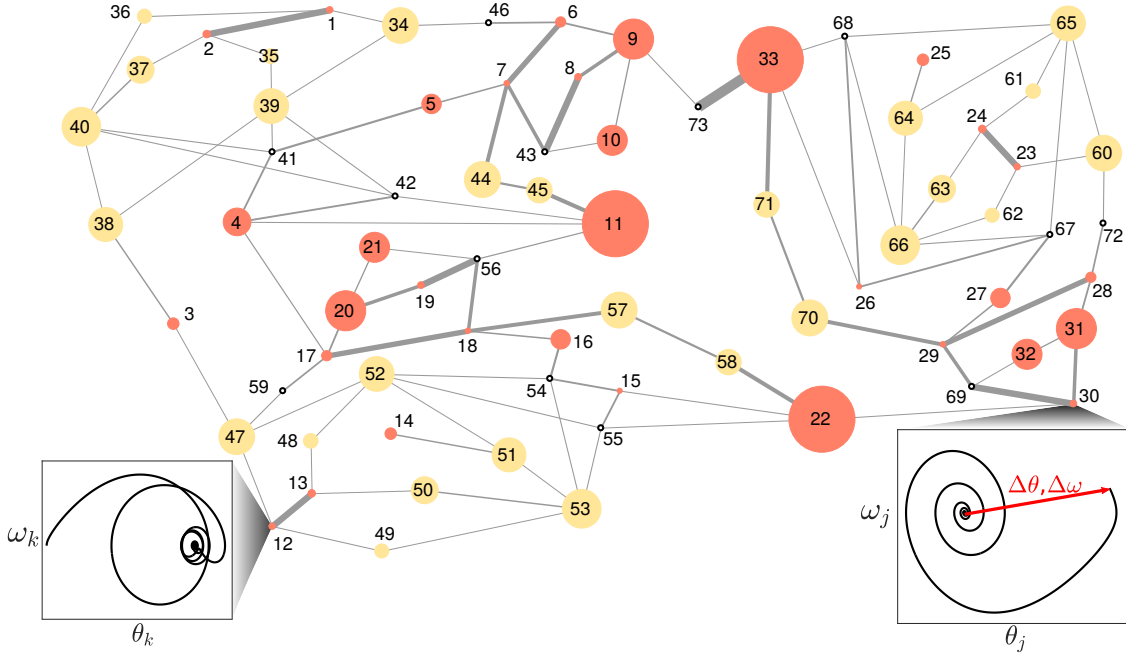


Figure 1. Sketch of the IEEE RTS-96 grid, consisting of 33 generator nodes labelled from 1 to 33 (full red circles), and 40 load nodes (full yellow/open white circles) labelled from 34 to 73. The open white circles refer to load nodes with vanishing mechanical power and the size of the full symbols has been scaled proportional to their mechanical power (for details, see section 2.3). The nodes are connected by 108 transmission lines, where the thickness of the lines mark the strength (modulus) of the respective complex admittances, which is defined by $[|(Y_0)_{jk}| + |(Y_0)_{kj}|]/2$, where $(Y_0)_{jk}$ are the elements of the admittance matrix, see section 2.1. In a fixed point state of the power flow dynamics, the frequencies at all nodes are equal, corresponding to a state of synchronous operation, where the differences $(\theta_j - \theta_k)$ between voltage phase angles at all node pairs (j, k) remain constant. After a perturbation of node j belonging to the attraction basin of the fixed point, this, as well as other nodes k , return to their stationary dynamics in the fixed point state. A corresponding perturbation of a node j is indicated by the red arrow, together with the subsequent trajectories of the phase angles and frequencies at this and another node k .

dynamics do not affect much the grid stability under stochastic power input [11]. With respect to the grid representation, often simplifications are made for specific purposes, e.g. by using artificial grid structures, and/or by taking real network graph structures, but neglecting heterogeneities in properties of generators, loads and transmission lines [7, 12, 13, 14]. A further simplification frequently made is the neglect of reactances between points of power production/consumption (internal nodes) and power injection/ejection (terminal nodes). These reactances can, however, be important, because they change the effective grid structure from a locally connected to a fully connected one.

In this work we are investigating power grid response to single-node perturbations by taking into account strong heterogeneities in line and node properties typically encountered at high-voltage transmission grid levels. For a faithful representation of these heterogeneities, we use the IEEE RTS-96 grid (reliability test system 96) [15], which is sketched in figure 1 together with the methodology used in this work. After perturbation of a node j in the grid, i.e. changes $\Delta\theta$ and Δf (or $\Delta\omega = 2\pi\Delta f$) of its voltage phase angle and frequency from

their values in a stable fixed point of synchronous grid operation, the subsequent responses of the phase angles and frequencies of all nodes are monitored. The range of considered perturbations covers all possible $\Delta\theta \in [-\pi, \pi[$, and frequencies in an interval ± 1 Hz with respect to the synchronous frequency, i.e. $\Delta f \in [-1 \text{ Hz}, 1 \text{ Hz}]$. This frequency range is quite wide in view of the range of primary control of up to 0.4 Hz.‡ As for quantifying grid stability against single-node perturbations, this can be defined by the probability of return to a fixed point of synchronous operation for the considered perturbation range, called basin stability [14, 17]. In practice, it matters also how long the grid needs to return to the vicinity of the synchronous state. We therefore characterise the grid stability not only by the probability of return but also by the return times for the perturbations belonging to the attraction basin of the fixed point. A similar concept has been recently introduced in [18].

In addition to getting insight into the basin stability and distribution of return times of a test grid reflecting real properties, a further goal of this work is to evaluate the relevance of the heterogeneities in transmission line and node features for estimating grid stability, e.g. for identifying possible trouble-causing nodes. To this end we compare our results to those obtained for simplified, homogenised grid properties, as they are sometimes used in case studies of grid stability. We furthermore investigate effects of reactances between internal and terminal nodes by using values derived from a method suggested in [9].

The paper is organised as follows. In section 2 we describe the modelling of the power grid structure (section 2.1) and of the power flow dynamics (section 2.2), and the parameters for simplified and extended variants of the IEEE RTS-96 grid (section 2.3). In section 3 we investigate the probabilities of return to the fixed point state of synchronous operation based on the basin stability measure introduced in [17]. The return times are studied in section 4 as an additional measure to characterise the grid response for perturbations in the attraction basin of a fixed point. For both the basin stability and return times we analyse the changes found upon homogenising node and line properties and/or when neglecting internal nodes. Our main results are summarised in section 5 together with a discussion of their consequences and impact for further studies.

2. Grid structure modelling and power flow dynamics

2.1. Grid structure modelling

A common representation of transmission lines in a power grid is given by the so-called Π -model [19], which is illustrated in figure 2(a) for a line between two nodes 1 and 2 (part enclosed by dashed lines). It consists of an admittance $y = g + ib$, with conductance g and susceptance b , and a line charging susceptance b_c represented by two capacitors in parallel to it. For representing a transformer with turn ratio r and phase shifting α , the model can be extended to the branch model, given by all elements shown in figure 2(a). For this branch model, the (complex) outgoing currents $I_{1\rightarrow}$ and $I_{2\rightarrow}$ leaving nodes 1 and 2 are linearly related

‡ Even in the 2006 European blackout, the largest frequency deviations were of the order of 1 Hz [16].

to the (complex) node voltages V_1 and V_2 ,

$$\begin{bmatrix} I_{1 \rightarrow} \\ I_{2 \rightarrow} \end{bmatrix} = \begin{bmatrix} y_{11} & y_{12} \\ y_{21} & y_{22} \end{bmatrix} \begin{bmatrix} V_1 \\ V_2 \end{bmatrix}, \quad (1)$$

where $y_{11} = (y + ib_c/2)/r^2$, $y_{12} = -ye^{i\alpha}/r$, $y_{21} = -ye^{-i\alpha}/r$, and $y_{22} = (y + ib_c/2)$. The relations for the Π -model of a transmission line are obtained by setting $r = 1$ and $\alpha = 0$, and in this case one has $y_{12} = y_{21}$ and $y_{11} = y_{22}$. Accordingly, one can assign a 2×2 admittance matrix to each transmission or transformer line in the power grid.

In a grid with N nodes, several lines can be connected to a node j , and we define I_j as the total current leaving this node, i.e. the sum of the currents flowing into the connected lines. Because all currents and voltages are linearly related, one can write

$$I = YV, \quad (2)$$

where $I = (I_1, \dots, I_N)^T$ and $V = (V_1, \dots, V_N)^T$ are the column vectors of node currents and voltages, respectively, and Y is an $N \times N$ admittance matrix. In general, one needs to consider also the effect of leakage currents at some nodes, which can be taken into account by a change of the diagonal elements of Y [20].

A further aspect is to consider impedances between the points of power generation/consumption and the points of power injection/ejection into/from the grid, as illustrated in figure 2(b). This amounts of extending the grid structure by adding an internal node (of power generation/consumption) to each node that after this addition represents a terminal node of power injection/ejection [9]. Each internal node is connected by one line with admittance y_j to the corresponding terminal node j [see also figure 2(b)].[§] With the zero current vector and voltage vector V for the passive terminal nodes in the extended grid, and the current vector I' and voltage vector V' for the internal nodes, the relation between voltages and currents becomes

$$\begin{bmatrix} I' \\ 0 \end{bmatrix} = \left\{ \begin{bmatrix} Y_d & -Y_d \\ -Y_d & Y_d \end{bmatrix} + \begin{bmatrix} 0 & 0 \\ 0 & Y \end{bmatrix} \right\} \begin{bmatrix} V' \\ V \end{bmatrix} = \begin{bmatrix} Y_d & -Y_d \\ -Y_d & Y + Y_d \end{bmatrix} \begin{bmatrix} V' \\ V \end{bmatrix}, \quad (3)$$

where Y_d is the diagonal matrix with elements $(Y_d)_{jj} = y_j$. Eliminating V by using the second line of the block-matrix equation (3), $V = (Y + Y_d)^{-1}Y_d V'$, the first line of (3) becomes

$$I' = Y'V', \quad (4)$$

where $Y' = Y_d - Y_d(Y + Y_d)^{-1}Y_d$. This reduction to an effective grid consisting of only the N internal nodes is commonly referred to as Kron reduction. By Kron reduction, nodes being connected in the original graph by a path of passive nodes become directly linked in the reduced graph [21]. Accordingly, the graph associated with equation (4) corresponds to a complete graph between the internal nodes.

In the following, we write all further equations for the grid model without consideration of the internal nodes, i.e. for the relation (2) between currents and voltages. The corresponding equations for the extended grid model with internal nodes are obtained by replacing Y with Y' and V with V' .

[§] The steady-state values of these admittances can be affected in transient time intervals by the armature reaction effect [19], which will not be considered here.

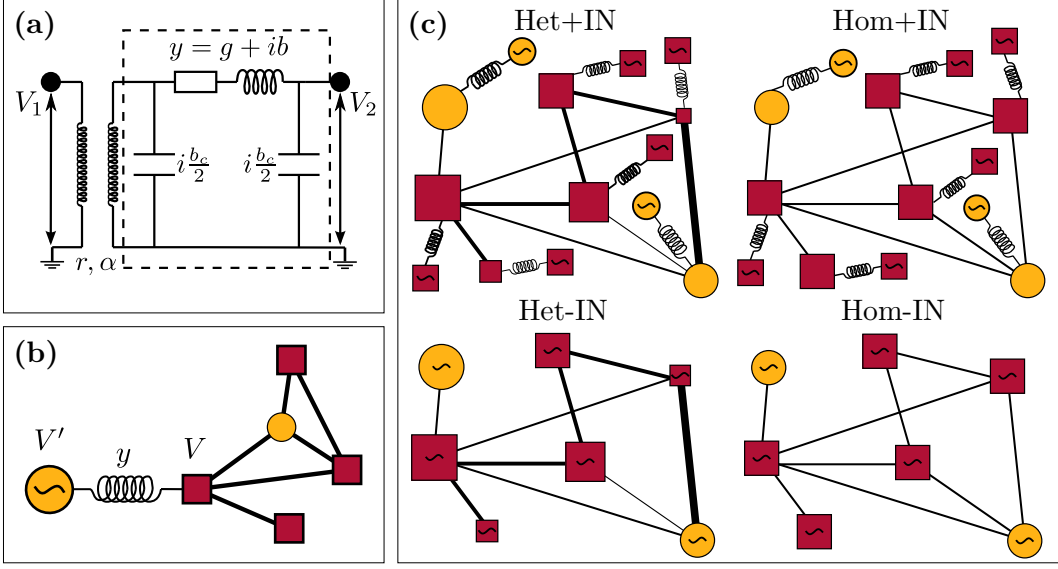


Figure 2. (a) Illustration of the branch model and Π -model (part enclosed in dotted lines) for transformer and transmission lines, respectively. (b) Illustration of an internal node (voltage V') and a terminal node (voltage V), together with their connecting admittance y . (c) Four different representations of the grid, where “Het” stands for the grid with heterogeneities in transmission line and node properties and “Hom” for homogenized transmission line and node properties (cf. section 2.3). The \pm IN indicates whether internal nodes are taken into account or not. In (b) and (c) nodes with a tilde would act as active nodes in the dynamical equation and can not be eliminated by Kron reduction, see section 2.1.

2.2. Power flow dynamics

In the synchronous state of a power grid, all nodal currents and voltages have a common harmonic time dependence, $I_j(t) = \text{Re}[I_j e^{-i\omega_r t}]$, $V_j(t) = \text{Re}[V_j e^{-i\omega_r t}]$, where $I_j = |I_j| e^{i\varphi_j}$ and $V_j = |V_j| e^{i\theta_j}$ are the complex amplitudes (or “phasors”), and ω_r is the common reference frequency of the generators. Generators and loads are in first place characterized by their power supply and consumption. It is thus common to rewrite the relation (2) in terms of powers $S_j = V_j I_j^* = P_j + iQ_j$, where I_j^* denotes the complex conjugate of I_j , and $P_j = \text{Re} S_j$ and $Q_j = \text{Im} S_j$ are the real and reactive electrical powers generated by node j ($P_j < 0$ if power is consumed). Eliminating the currents with the help of equation (2), $S_j = V_j I_j^* = \sum_k V_j V_k^* Y_{jk}^*$, and writing $Y_{jk} = |Y_{jk}| \exp[i(\gamma_{jk} + \pi/2)]$,^{||} one obtains

$$P_j = \sum_k |V_j| |V_k| |Y_{jk}| \sin(\theta_j - \theta_k - \gamma_{jk}), \quad (5)$$

$$Q_j = \sum_k |V_j| |V_k| |Y_{jk}| \cos(\theta_j - \theta_k - \gamma_{jk}). \quad (6)$$

Balancing these electrical powers with the “mechanical powers” $S_j^{(m)} = P_j^{(m)} + iQ_j^{(m)}$ determines the steady state of the power grid. The corresponding equations are called power flow equations. In power flow modelling, values $P_j^{(m)}$ and $|V_j|$ are usually given for generator

^{||} The shift of $\pi/2$ in this definition of the phase angle γ_{jk} is introduced to yield a sine function in the subsequent equation (7), which then has the common form of a Kuramoto model of second order [22, 23, 24].

nodes and values $P_j^{(m)}$ and $Q_j^{(m)}$ for load nodes.

For describing the mechanical coupling to the electricity grid, we use the synchronous machine model for both generators and loads with constant voltage moduli $|V_j|$ [9]. If the frequency of a synchronous machine deviates from ω_r , the voltage phase angles θ_j become time-dependent and evolve in time according to the swing equations [19, 25]

$$H_j \ddot{\theta}_j + D_j \dot{\theta}_j = P_j^{(m)} - P_j = P_j^{(m)} - \sum_k K_{jk} \sin(\theta_j - \theta_k - \gamma_{jk}) . \quad (7)$$

Here, $K_{jk} = |V_j||V_k||Y_{jk}|$ are the coupling constants, and H_j and D_j are inertia and damping constants, respectively. The inertia constant H_j is connected with the rotating mass of a motor or conventional generator. The constants D_j effectively include both electro-dynamical and mechanical damping effects, as well as primary control measures [26]. Because only differences between phase angles appear in equation (7), the dynamics are invariant under a constant phase shift $\theta_j \rightarrow \theta_j + \beta$. For uniqueness, we have set $\theta_1 = 0$ as a reference angle.

Fixed points of equation (7) correspond to a stationary synchronous state described by equations (5) and (6), where mechanical and electrical power are balanced ($P_j^{(m)} = P_j$). In this state, the frequency deviations $\omega_j = \dot{\theta}_j$ from the reference frequency ω_r become zero and the phase angles stay constant. Because equations (5) and (6) are non-linear in the θ_j , there can be more than one fixed point [27, 28]. As our reference fixed point, we take the solution of equations (5) and (6) obtained by a Newton-Raphson method with starting angles $(\theta_1, \dots, \theta_N) = (0, \dots, 0)$, yielding the fixed point vector $(0, \theta_2^*, \dots, \theta_N^*)$. If the provided/consumed mechanical power $P_j^{(m)}$ deviates from the electrical power P_j , the frequencies $\omega_j = \dot{\theta}_j$ are driven away from zero and the phase angles from their fixed point state.

2.3. Parameters for extended and simplified variants of the IEEE RTS-96 grid

For our analysis, we use the IEEE RTS-96 grid with structure shown in figure 1, where for each node is listed a load contribution $\Pi_j^{(l)} \leq 0$ and for a subset an additional generator contribution $\Pi_j^{(g)} > 0$. The latter nodes are specified as generator nodes in the RTS-96 grid and the other as load nodes. The $N_g = 33$ generator nodes are numbered 1 to 33 and the $N_l = 40$ load nodes 34 to 73. Setting $\Pi_j^{(g)} = 0$ for the load nodes, the $P_j^{(m)}$ are fixed by $P_j^{(m)} = \Pi_j^{(g)} + \Pi_j^{(l)}$. Furthermore, the $|V_j|$ are listed for generator nodes, and the $Q_j^{(m)}$ for load nodes. For each lines in the network, the admittances [see equation (1)], as well as the leakage currents (or shunt elements) are provided, i.e. all information to calculate the elements Y_{jk} of the admittance matrix in equation (2). Altogether this allows one to determine stationary states based on the power flow equations (5) and (6).

For solving the dynamic equations (7), the damping and inertia constants D_j and H_j are also needed. Corresponding values are not listed for the IEEE RTS-96 grid (except H_j for generator contributions). To assign values to these constants, we use estimates given in Ref. [29], resulting in D_j being all the same, namely $D_j \cong 13$ MWs, and H_j being proportional to the $P_j^{(m)}$ beyond a minimum value, $H_j = \max(0.064 \text{ MWs}^2, 2.54 \times 10^{-4} P_j^{(m)})$. Moreover, when taking into account internal nodes, the admittances y_j between

internal and terminal nodes are needed. To specify them, we use the empirical relation $y_j = 92.8(P_j^{(m)})^{-1.3}$ [29].

As for the units, powers $S_j = P_j + iQ_j$ are expressed in terms of a power base $P_b = 100$ MW. Times (frequencies) are given in units of seconds (Hertz). Accordingly, the units for the coupling constants K_{jk} , the damping constants D_j and the inertia constants H_j in equation (7) are $P_b = 100$ MW, 100 MWs and 100 MWs^2 , respectively. Voltages are given in a so-called per-unit system (p.u.), to avoid a modelling of different voltage levels in the grid. A voltage base V_b is specified as the nominal value for each voltage level. Admittances Y_{jk} then have units $Y_b = P_b/V_b^2$. In the following, all quantities are given in dimensionless numbers with respect to these units.

Taking these properties altogether, one arrives at a model that incorporates the internal nodes as well as the heterogeneities both in the nodes, i.e. the different values of $P_j^{(m)}$, $Q_j^{(m)}$ and $|V_j|$, and in the transmission lines, i.e. the different values of the admittances Y_{jk} . We refer to this model as “Het+IN”.

To investigate the impact of simplifications of the network structure on the evaluation of grid stability, we consider the following model variants. In the first variant, referred to as “Het-IN”, the internal nodes are neglected. As a consequence, there are no passive nodes and, instead of the admittance matrix Y' , the admittance matrix Y is used, see equations (2) and (4).

Two further variants “Hom±IN” (with and without internal nodes) are obtained by homogenising the transmission line properties as well as the generated and consumed powers. Corresponding homogeneous power grid structures have been investigated in various previous studies [7, 12, 13, 14, 30, 31], typically for the case of loss-free transmission lines. For the homogenisation, we here also consider a loss-free situation, i.e. we neglect the resistances of the transmission lines and the leakage currents. We additionally set $r = 1$ for the transformer lines (transformer phase shifts α are zero in the IEEE RTS-96 grid). Then the arithmetic mean of the line admittances is assigned to all transmission lines. As for the powers $P_j^{(m)}$, we assign to the generator nodes their average power ($\bar{P} = \sum_{j=1}^{N_g} P_j^{(m)}/N_g$) and to the load nodes the one ensuring a balance between generated and consumed power ($-\bar{P}N_g/N_l$).¶ Analogously, we take the arithmetic means for setting the voltage moduli of the generator nodes and for setting the reactive power of the load nodes.

All four models, Het±IN and Hom±IN are illustrated in figure 2(c) and the relevant parameters entering equation (7) are plotted in figure 3. For the heterogeneous models, the $P_j^{(m)}$ [figure 3(a)] and H_j [figure 3(b)] cover a quite broad range (black circles), while in the homogenised models, two different fixed values for generator and load nodes are given in each case (green circles). Let us note that seven of the generator nodes have an “effective load power” $P_j^{(m)} < 0$, because $\Pi_j^{(g)} < |\Pi_j^{(l)}|$. Moreover, thirteen of the load nodes have $P_j^{(m)} = \Pi_j^{(l)} = 0$ and therefore act like passive nodes in the synchronous state of operation, but not in the dynamical case with an overall imbalance of mechanical and electrical power.

¶ Let us note that a corresponding balance under consideration of losses, i.e. when keeping the resistances of the lines, can usually be ensured only, if one generator node is allowed to exhibit a mechanical power different from the other generator nodes. Accordingly, in that case one would not consider a fully homogenised grid.

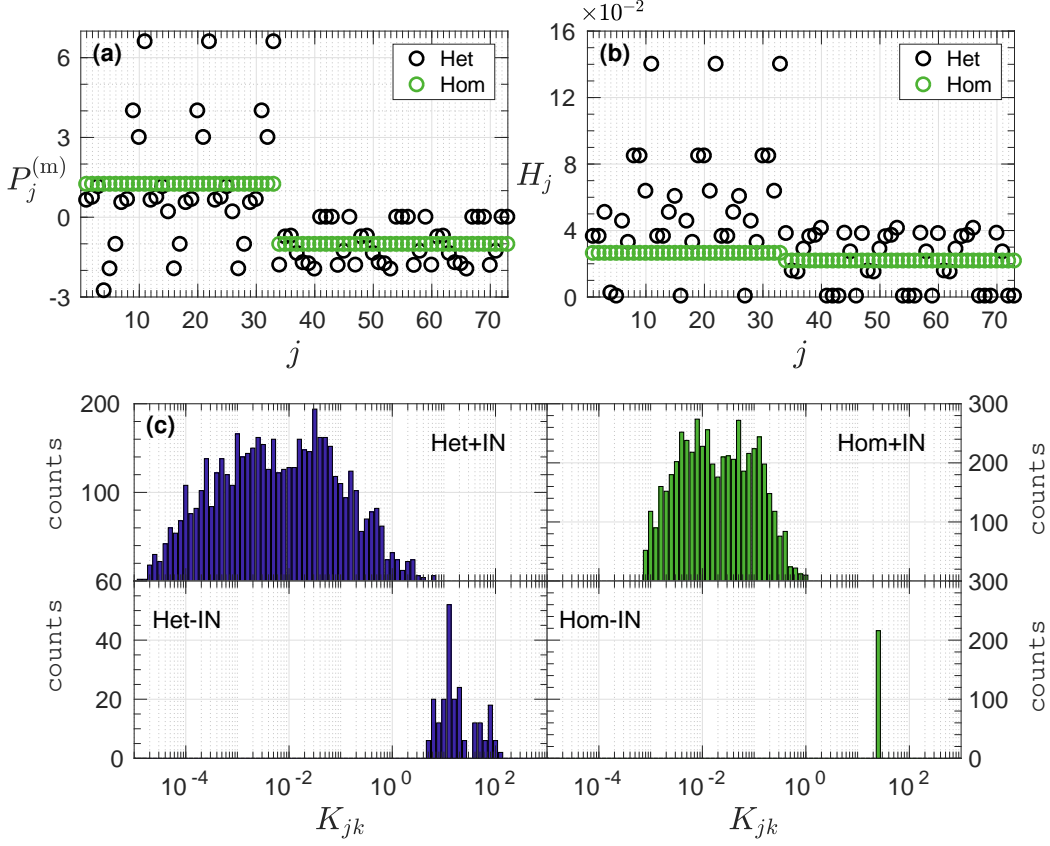


Figure 3. (a) Mechanical powers $P_j^{(m)}$ for all nodes j in the heterogeneous models (black bullets) and the homogenised counterparts (green bullets). (b) Corresponding inertia constants H_j for all nodes. (c) Histograms of the coupling constants K_{jk} for each of the four models sketched in figure 2(c) without diagonal elements.

These load nodes are marked by open circles in figure 1.

In figure 3(c), histograms of the coupling constants K_{jk} are shown for the four models. As can be seen from this figure, the heterogeneous models yield distributions spanning a broader range, including those obtained for the homogeneous counterparts. For the models Het-IN and Hom-IN, the coupling matrix K resembles the adjacency matrix of the network without internal nodes, i.e. it has non-zero entries only for transmission lines connecting two nodes. There are in total 108 of these entries for the IEEE RTS-96 grid. For the models Het+IN and Hom+IN with internal nodes, K is a full matrix due to the Kron reduction. This matrix has $73 \times 73 = 5329$ non-zero entries, resulting in the different numbers of counts in the corresponding histograms in figure 3(c). Moreover, in the synchronous state, equation (5) must be fulfilled for the same $P_j^{(m)}$, implying that the couplings $K_{jk} = |V_j||V_k||Y_{jk}|$ for the models without internal nodes, where $Y_{jk} \neq 0$ only for nodes connected by transmission lines, must be in general larger than that of the corresponding models with internal nodes. Accordingly, their histograms are centred around coupling constants larger than that of their counterparts.

Let us note also, that, despite of the homogenising, the histogram for the Hom+IN model exhibits an appreciable width. This is because the matrix elements of Y' in equation (4) vary due to the inhomogeneity in the link topology of the grid, which is present also for the homogenised variants. Even for the Hom-IN model, the width is not zero, because the K_{jk} depend also on the voltage moduli, which in the fixed point state vary slightly for the load nodes.

3. Basin stability

If mechanical and electrical powers are balanced, all phases have the same angular velocity $\dot{\theta}_1 = \dot{\theta}_2 = \dots = \dot{\theta}_N = \omega_r$ in the fixed point state. There is another type of stationary solutions of equation (7), which correspond to limit cycles [14], where phase angles and frequencies of nodes follow closed trajectories. These limit cycles imply undesirable frequency variations. Depending on the amplitude of a perturbation from the fixed point state, the system either returns to this point or turns into the undesirable state of asynchronous voltage phase dynamics, which we refer to as “grid failure” in the following.

As a measure for the stability of the synchronous fixed point state one can take the probability of return to this state after perturbations $(\Delta\theta, \Delta\omega)$ of single nodes. The $(\Delta\theta, \Delta\omega)$ are drawn from a probability density $p_0(\Delta\theta, \Delta\omega)$, which we take to be uniform in the region $\mathcal{R} = [-\pi, \pi] \times [-2\pi, 2\pi]$. After a perturbation of node j , the probability S_j of the grid to return to the fixed point state is then given by

$$S_j = \int d(\Delta\theta) d(\Delta\omega) p_0(\Delta\theta, \Delta\omega) \chi_j(\Delta\theta, \Delta\omega) = \frac{1}{8\pi^2} \int_{\mathcal{R}} d(\Delta\theta) d(\Delta\omega) \chi_j(\Delta\theta, \Delta\omega). \quad (8)$$

Here $\chi_j(\Delta\theta, \Delta\omega)$ is an indicator function, being one if the grid returns to the fixed point after a perturbation $(\Delta\theta, \Delta\omega)$ of node j , and zero otherwise. We define the set of points $\mathcal{B}_j = \{(\Delta\theta, \Delta\omega) | \chi_j(\Delta\theta, \Delta\omega) = 1\}$ as the “attraction basin” of the fixed point, where one should keep in mind that we consider single node perturbations and not the full $(2N)$ -dimensional phase space around the fixed point. For the uniform distribution $p_0(\Delta\theta, \Delta\omega)$, S_j in equation (8) equals the fraction of return points in \mathcal{R} , which has been referred to as “basin stability” [17]. The probability of grid failure is $(1 - S_j)$.

To determine the basin stabilities S_j , we scan the perturbation region \mathcal{R} by using a fine raster grid of spacing $(\delta\theta, \delta\omega) = (0.1, 0.1)$. For each point $(\Delta\theta, \Delta\omega)$ in this grid, we solved equation (7) for the initial conditions $(\theta_j, \omega_j) = (\theta_j^* + \Delta\theta, \Delta\omega)$ and $(\theta_k, \omega_k) = (\theta_k^*, 0)$ for all $k \neq j$. This is done numerically by using a Runge-Kutta solver of fourth order.

The grid is considered to have returned to the fixed point [$\chi_j(\Delta\theta, \Delta\omega) = 1$], if there exists a time beyond which the magnitudes of all frequencies $\omega_k(t)$ remain below a threshold ϵ , i.e. when $|\omega_k(t)| < \epsilon$ for long times and all k . Otherwise, the grid is considered to have turned into a limit cycle [$\chi_j(\Delta\theta, \Delta\omega) = 0$]. The threshold is set as $\epsilon = 0.01$, implying that frequency deviations below ϵ corresponds to values well below the onset of primary control measures [typically starting at deviations $\omega/(2\pi)$ of about 10 mHz]. In practice, we have taken a total simulation time of 25 seconds for the analysis of $\chi_j(\Delta\theta, \Delta\omega)$. We carefully checked that the

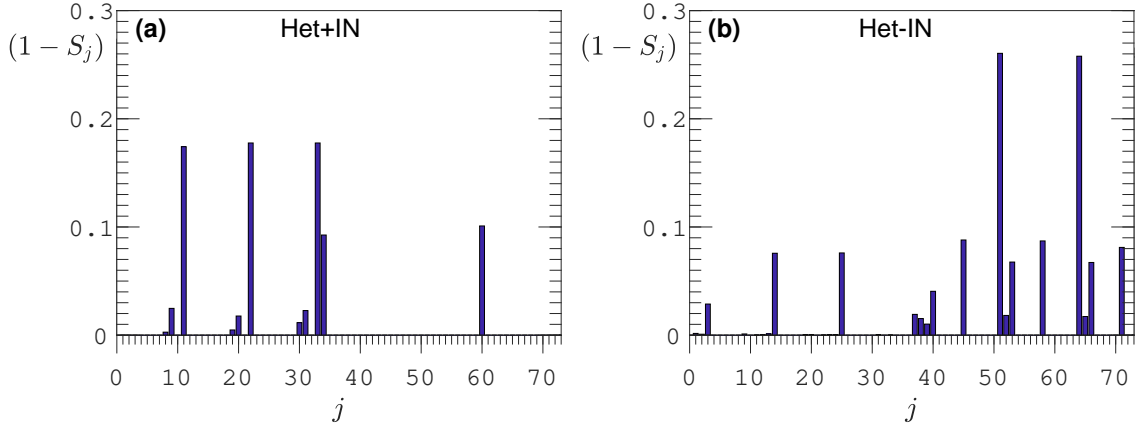


Figure 4. Probabilities $(1 - S_j)$ of grid failure after perturbing node j [see equation (8)] for models (a) Het+IN and (b) Het-IN.

results did not change when increasing the total simulation time. The integral in equation (8) is evaluated numerically by summing over the points of the raster grid.

Figure 4 shows the probability $(1 - S_j)$ of grid failure after a perturbation of node j for models (a) Het+IN and (b) Het-IN. For the homogeneous models, we always found that the grid returns to the fixed point state for perturbations in \mathcal{R} , i.e. $(1 - S_j) = 0$ for all j . Comparing the results for the models Het+IN and Het-IN, we see that for the model Het+IN less perturbed nodes j can lead to grid failure. This can be understood by the fact that the coupling matrix for the Het+IN model represents a complete graph and accordingly a perturbation of node j becomes rapidly distributed over all other nodes. For the Het-IN model, by contrast, node j has only a few nearest-neighbour nodes (see also figure 1) and a perturbation can have a stronger impact on the loss of grid stability. The change of the coupling structure is also reflected in the fact that almost all of the perturbed nodes in model Het+IN, which can cause grid failure, do never lead to grid failure in model Het-IN (for perturbation in \mathcal{R}).

In the Het+IN model, the nodes with high grid failure probabilities $(1 - S_j)$ always have relatively high values $|P_j^{(m)}|$. In particular, the three nodes 11, 22, and 33 with the highest $(1 - S_j)$ have also the largest $|P_j^{(m)}|$. In the Het-IN model this correlation is not present. Interestingly, there the neighbours of the nodes constituting dead ends in the grid topology exhibit the highest grid failure probabilities, see the $(1 - S_j)$ values in figure 4(b) for the nodes 51 and 64, which are the neighbours of the dead-end nodes 14 and 25 (cf. figure 1). The dead-end nodes themselves belong to the group of nodes with highest failure probabilities larger than 7%. These findings are in agreement with those reported in [14]. There, a grid structure corresponding to the homogenised variant without internal nodes was analysed, but with an about 100 times larger range of initial frequency perturbations $\Delta\omega$.

However, nodes 45, 58, and 71 in figure 4(b) exhibit also grid probabilities larger than 7%. As can be seen from figure 1, each of these nodes has only two neighbours and one of them has high $P_j^{(m)}$ [see also figure 3(a)] and accordingly high inertia $H_j \propto P_j^{(m)}$ [see figure 3(b)]. The high inertia implies that the corresponding nodes react very slowly in response to perturbations at the neighbouring node, i.e. the three nodes 45, 58, and 71 can

be considered as “effective dead ends”. That in this case perturbations at the effective dead end nodes themselves, rather than their neighbours, most likely lead to grid failure, can be understood from the fact, that the neighbouring nodes with high inertia act like “fixed” rather than “loose” ends.

Overall, the perturbed nodes that can cause grid failure in figures 4(a) and (b) are smaller in number than the ones showing always return to the synchronous fixed point state. The maximal probabilities for grid failure are below 20% for model Het+IN and 30% for model Het-IN, implying that for the corresponding perturbed nodes the attraction basins \mathcal{B}_j cover more than 80% and 70% of \mathcal{R} , respectively. In the following we will refer to the nodes with $S_j < 1$ as “basin-escapable” (BE) nodes.

4. Return times

Since all single node perturbations for the homogenised models and most of them for the heterogeneous models lead to return of the power grid to the stable fixed point state, the grid stability should be assessed in more detail. In fact, not only the return to a synchronous state of operation matters, but also the time needed for this return after a perturbation. Therefore, we introduce a return time $\tilde{t}_{jk}(\Delta\theta, \Delta\omega; \epsilon)$ as the minimum time for $|\omega_k(t)| < \epsilon$ to hold for all $t > \tilde{t}_{jk}(\Delta\theta, \Delta\omega; \epsilon)$, after node j is perturbed with an amplitude $(\Delta\theta, \Delta\omega)$. In case the grid state turns into a limit cycle for the perturbation $(\Delta\theta, \Delta\omega)$, $\tilde{t}_{jk}(\Delta\theta, \Delta\omega; \epsilon)$ is assigned infinity for all k . In this way, the \tilde{t}_{jk} [for all $(\Delta\theta, \Delta\omega)$ and all k] contain also the information of S_j in equation (8).

Figure 5(a) shows a part of a representative trajectory of $|\omega_3(t)|$ if node 9 is perturbed ($j = 9, k = 3$) with $(\Delta\theta, \Delta\omega) = (2.5, 3.1)$; the full trajectory over the entire simulation time is displayed in the inset. Similar trajectories are obtained for other node pairs. As can be seen from this figure, $|\omega_3(t)|$ shows oscillations and one can subdivide the trajectory into oscillation branches between successive zero crossings of $\omega_3(t)$. These zero crossings correspond to the minima (“cusps”) in the semi-logarithmic representation of $|\omega_3(t)|$ in figure 5(a). The exact value $(-\infty)$ of these minima is, however, not fully approached due to the finite time iteration step in the numerics. For illustration, we have indicated one oscillation branch by the dashed vertical lines in figure 5(a).

The appearance of the oscillation branches can lead to jumps in the functions $\tilde{t}_{jk}(\Delta\theta, \Delta\omega; \epsilon)$, because, if changing $(\Delta\theta, \Delta\omega)$ slightly, the crossing of the threshold ϵ can occur in two different oscillation branches. This effect is demonstrated in figure 5(b). For smoothing the dependence of the return times on the initial perturbations $(\Delta\theta, \Delta\omega)$, we average the \tilde{t}_{jk} over a number of $(2n + 1)$ equidistantly spaced thresholds around a reference value ϵ , yielding

$$t_{jk}(\Delta\theta, \Delta\omega) = \frac{1}{2n + 1} \sum_{m=-n}^n \tilde{t}_{jk}(\Delta\theta, \Delta\omega; \epsilon + m\Delta\epsilon). \quad (9)$$

For ϵ we take the same value $\epsilon = 0.01$ as in the previous section for the stability basin analysis

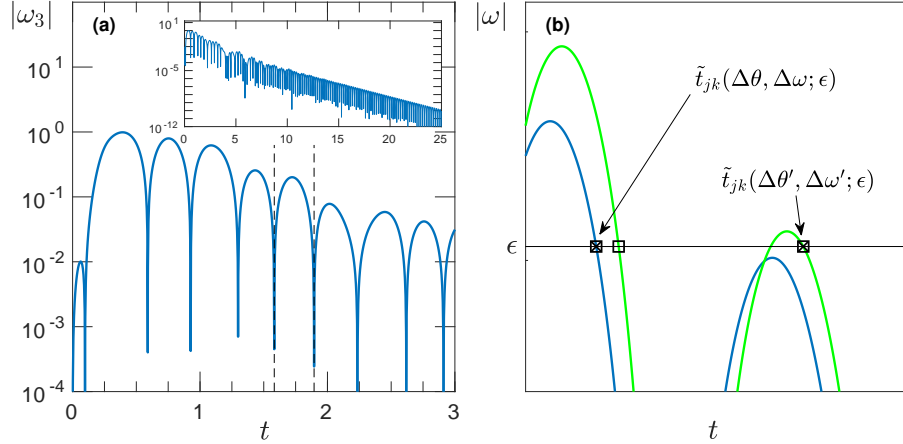


Figure 5. (a) Part of the trajectory $|\omega_3(t)|$ of node $k = 3$ if node $j = 9$ is perturbed with $\Delta\theta = 2.5$ and $\Delta\omega = 3.1$. The vertical dashed lines indicate one oscillation branch between zero crossings of $\omega_3(t)$ (see text) and the inset displays the trajectory over the full simulation time. (b) Illustration of a jump in the return times $\tilde{t}_{jk}(\Delta\theta, \Delta\omega; \epsilon)$ upon changing the initial perturbation $(\Delta\theta, \Delta\omega)$ to a nearby $(\Delta\theta', \Delta\omega')$: The blue line marks the trajectory of $|\omega_k(t)|$ for $(\Delta\theta, \Delta\omega)$ and the green one for $(\Delta\theta', \Delta\omega')$. For the blue line, $|\omega_k(t)|$ remains below the threshold ϵ (horizontal line) after the time $\tilde{t}_{jk}(\Delta\theta, \Delta\omega; \epsilon)$ (point marked by the crossed square). For the green line, the corresponding intersection of $|\omega_k(t)|$ with the horizontal line in the respective oscillation branch (point marked by the open square) does not give the correct return time. This is because in the successive oscillation branch the local maximum of the trajectory exceeds ϵ . The correct return time for the green line thus is $\tilde{t}_{jk}(\Delta\theta', \Delta\omega'; \epsilon)$ as indicated in the figure (point marked by the crossed square). Due to the change of the oscillation branch, $\tilde{t}_{jk}(\Delta\theta', \Delta\omega'; \epsilon)$ is not close to $\tilde{t}_{jk}(\Delta\theta, \Delta\omega; \epsilon)$.

and set $n = 3$ and $\Delta\epsilon = 1.4 \times 10^{-3}$.⁺

As an example, we show in figure 6 the return times $t_{jk}(\Delta\theta, \Delta\omega)$ of a node k after a perturbation of another node j in the Het+IN model, (a) in a surface plot and (b) in a colour-coded 2d-density plot. In the attraction basin \mathcal{B}_j , the $t_{jk}(\Delta\theta, \Delta\omega)$ become longer with increasing distance from the fixed point, e.g. the Euclidean distance $(\Delta\theta^2 + \Delta\omega^2)^{1/2}$. Points in the perturbation region \mathcal{R} leading to grid failure are marked black. Far from the fixed point, they typically form a connected domain. Note that the coloured stripe close to $\Delta\theta = \pi$ at the right side in figure 6(b) is connected to the corresponding part at the left side close to $\Delta\theta = -\pi$. However, in the transitory region between this domain and the core of the attraction basin, a closer inspection, with a finer resolution $(\delta\theta, \delta\omega)$ of the raster grid reveals that the grid stability becomes very sensitive to the initial perturbation, see figure 6(c). This reflects a kind of chaotic behaviour, i.e. nearby points $(\Delta\theta, \Delta\omega)$ can give different $\chi_j(\Delta\theta, \Delta\omega) \in \{0, 1\}$. For points with $\chi_j(\Delta\theta, \Delta\omega) = 1$ (return to the fixed point) in the transitory region, the $t_{jk}(\Delta\theta, \Delta\omega)$ can change rapidly between small and large values.

⁺ If one would be interested only in the grid return times (see below), an alternative way to obtain smoothly varying times is to consider the energy $E = \sum_j \frac{1}{2} H_j \omega_j^2 + \sum_j \sum_k \frac{1}{4} K_{jk} \cos(\theta_j^* - \theta_k^* - \gamma_{jk}) [(\theta_j - \theta_j^*) - (\theta_k - \theta_k^*)]^2$ of coupled harmonic oscillators, which characterises the system in the neighbourhood of the fixed point, see equation (7). If the phase space trajectory $\{(\theta_j(t), \omega_j(t))\}$ enters the nearest neighbourhood, this energy decreases monotonically with time t .

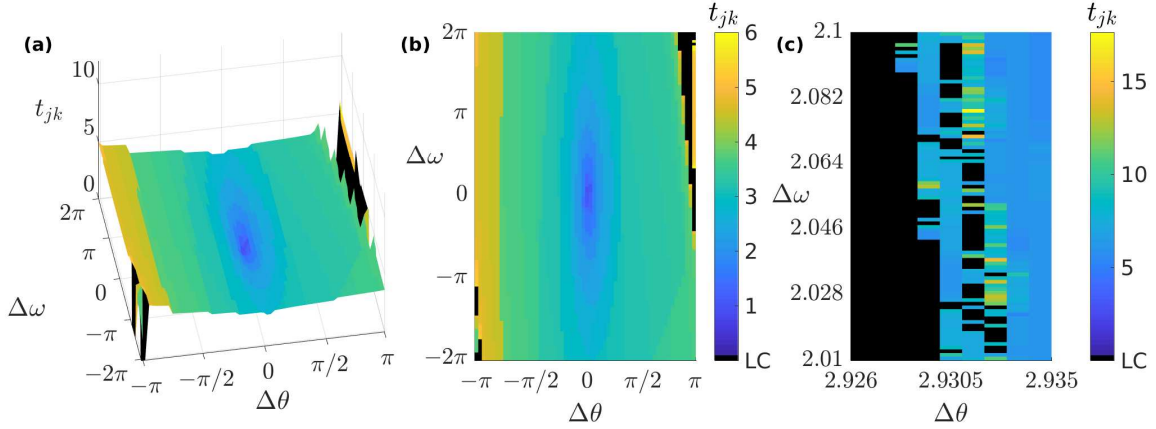


Figure 6. Return times $t_{jk}(\Delta\theta, \Delta\omega)$ of node $k = 3$ after initial perturbations $(\Delta\theta, \Delta\omega)$ of node $j = 9$, (a) in a surface plot and (b) in a colour-coded 2d-density plot representation. (c) Part of the 2d-density plot scanned with a finer raster grid resolution showing a chaotic behaviour in the transitory region between fixed point and limit cycle.

4.1. Mean grid and node return times

The $t_{jk}(\Delta\theta, \Delta\omega)$ contain detailed information on local return times, including the basin stability S_j of the perturbed node j . The latter quantifies how disturbing a node j is for the overall grid stability. For perturbations belonging to the attraction basins \mathcal{B}_j , the $t_{jk}(\Delta\theta, \Delta\omega)$ further allow us to quantify (i) how disturbing a node j is for sufficiently fast return to the fixed point, and (ii) how susceptible a node k is to a perturbation of any node in the grid (including the node k itself). To this end, we introduce two quantities. The first is the grid return time $t_j^{\text{grid}}(\Delta\theta, \Delta\omega)$, which is the maximum return time of all nodes k under a perturbation $(\Delta\theta, \Delta\omega)$ of node j , that means it is the time for the entire grid to return to the state of synchronous operation,

$$t_j^{\text{grid}}(\Delta\theta, \Delta\omega) = \max_k \{t_{jk}(\Delta\theta, \Delta\omega) | (\Delta\theta, \Delta\omega) \in \mathcal{B}_j\}. \quad (10)$$

The second quantity is the node return time $t_k^{\text{node}}(\Delta\theta, \Delta\omega)$. This is defined as the maximum return time of node k under a perturbation $(\Delta\theta, \Delta\omega)$ of any of the nodes j ,

$$t_k^{\text{node}}(\Delta\theta, \Delta\omega) = \max_j \{t_{jk}(\Delta\theta, \Delta\omega) | (\Delta\theta, \Delta\omega) \in \mathcal{B}_j\}. \quad (11)$$

Figure 7 shows an example for grid return times $t_j^{\text{grid}}(\Delta\theta, \Delta\omega)$ for the same perturbed node and the four model variants. Strong differences can be seen between the heterogeneous models Het \pm IN and their homogenised counterparts Hom \pm IN, and smaller differences between the models with and without internal nodes. The typical grid return times for the Het \pm IN models vary from 1 to 12 seconds and are significantly larger than for the Hom \pm IN models showing variations between 1 and 5 seconds. As already mentioned above, in the Het \pm IN models, certain initial perturbations $(\Delta\theta, \Delta\omega)$ lead to grid failure (points marked in black), while for the Hom \pm IN models the grid returns to the state of synchronous operation for all initial perturbations $(\Delta\theta, \Delta\omega) \in \mathcal{R}$. The main effect of including the internal nodes for both the heterogeneous and homogenized models shows up in a weaker dependence of

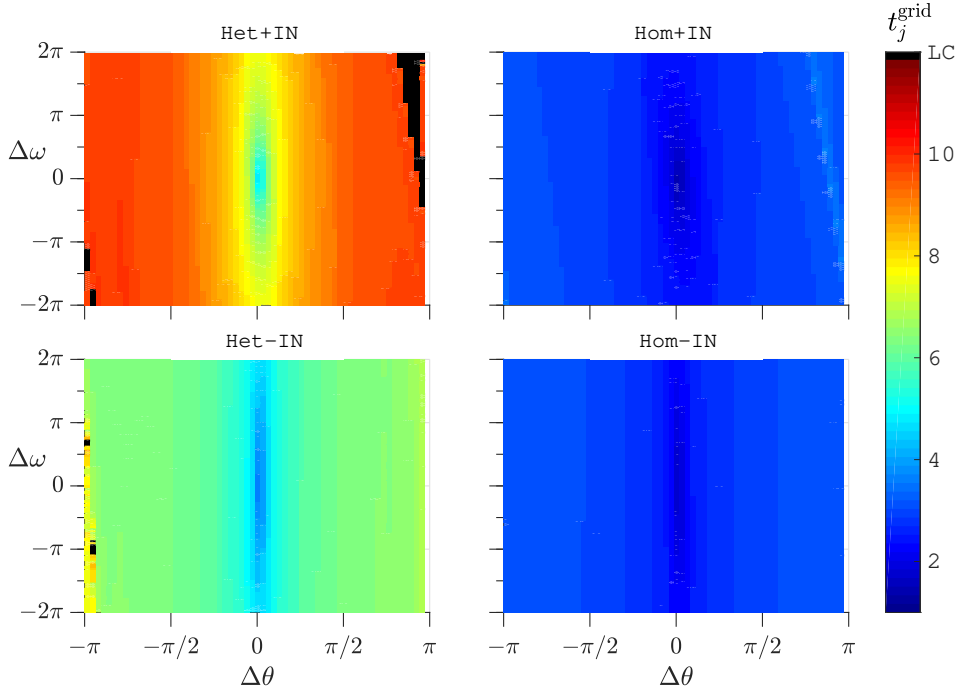


Figure 7. Surfaces of grid return times $t_j^{\text{grid}}(\Delta\theta, \Delta\omega)$ [equation (10)] for $j = 9$ and the four model variants in a density plot representation. Initial perturbations $(\Delta\theta, \Delta\omega)$ in the heterogeneous models leading to grid failure are marked black.

the times on the initial frequency perturbation $\Delta\omega$, as it is reflected in the more stripe-like pattern seen for the Het-IN and Hom-IN models compared to the Het+IN and Hom+IN models. Furthermore, we note that the transitory region of chaotic-like return time variations, as discussed in connection with figure 6, is typically more pronounced and extended for the Het-IN model. As for the node return times $t_k^{\text{node}}(\Delta\theta, \Delta\omega)$, a similar behaviour is obtained, with the same typical differences between the heterogeneous and homogeneous models and between the variants with and without internal nodes.

To characterise the nodes independent of the initial perturbations, an obvious way is to introduce the grid and node return times maximised over all $(\Delta\theta, \Delta\omega)$ in the respective attraction basins:

$$T_j^{\text{grid}} = \max_{(\Delta\theta, \Delta\omega) \in \mathcal{B}_j} \{t_j^{\text{grid}}(\Delta\theta, \Delta\omega)\}, \quad (12)$$

$$T_k^{\text{node}} = \max_{(\Delta\theta, \Delta\omega) \in \mathcal{B}} \{t_k^{\text{node}}(\Delta\theta, \Delta\omega)\}. \quad (13)$$

Here, $\mathcal{B} = \bigcap_j \mathcal{B}_j$ is the attraction basin for all possible single-node perturbations in \mathcal{R} irrespective of $(\Delta\theta, \Delta\omega)$ and the perturbed node j . In the Hom \pm IN models, we find $T_j^{\text{grid}} \simeq 4$ for all nodes, while in the Het \pm IN models strong variations of T_j^{grid} from node to node occur. For the BE nodes, i.e. the nodes that can cause grid failure, these times can be as large as 20. However, the determination of the T_j^{grid} for these BE nodes (and all T_k^{node}) needs to be considered with caution, because their values were seen to depend on the resolution of the raster grid. This effect is associated with the chaotic-like dependence of the $t_{jk}(\Delta\theta, \Delta\omega)$ on $(\Delta\theta, \Delta\omega)$ in the transitory regions between the limit-cycle domains and the cores of

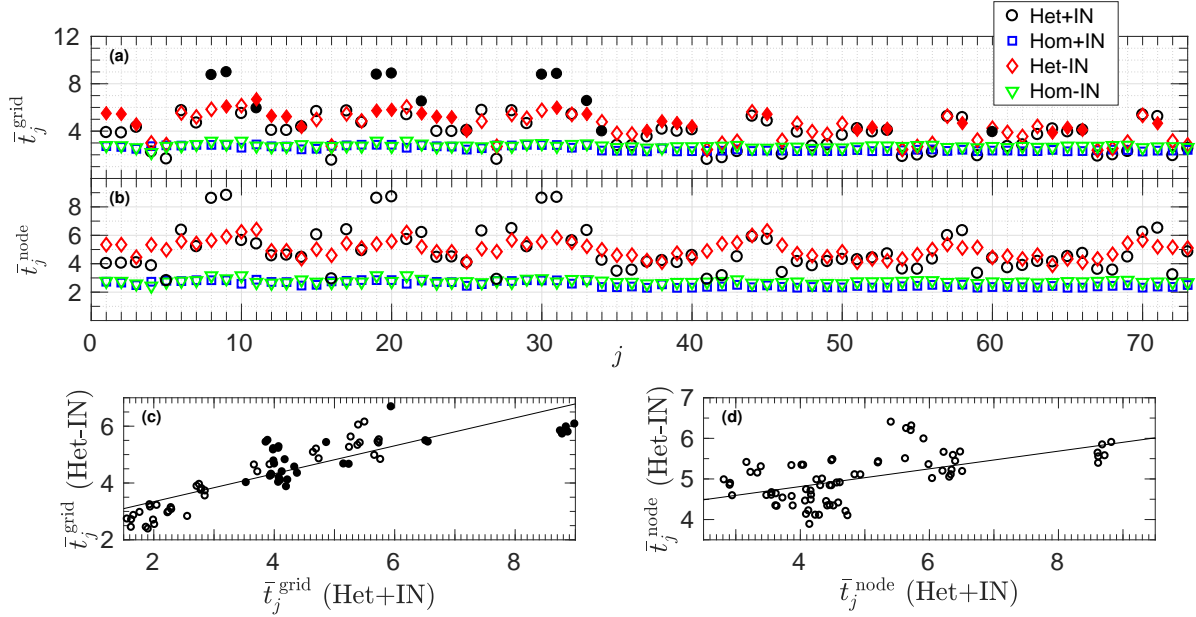


Figure 8. (a) Mean grid return times and (b) mean node return times for each node j and the four model variants. A correlation between the mean return times of the Het+IN and Het-IN models is tested in scatter plots, (c) for the grid return times, and (d) for the node return times. Lines in (c) and (d) correspond to least square fits and the correlation coefficients are $R \cong 0.85$ and $R \cong 0.56$ respectively. In parts (a) and (c) the BE nodes are marked by full symbols.

the attraction basins that we discussed above in connection with figure 6. Even larger values for the T_j^{grid} may be obtained when increasing the resolution beyond the finest one $(\delta\theta, \delta\omega) = (0.1, 0.1)$ used in our analysis.

To ensure robustness of our findings with respect to the raster grid resolution, we introduce the mean grid and node return times

$$\bar{t}_j^{\text{grid}} = \frac{1}{N_{B_j}} \int_{B_j} d(\Delta\theta) d(\Delta\omega) t_j^{\text{grid}}(\Delta\theta, \Delta\omega), \quad (14)$$

$$\bar{t}_k^{\text{node}} = \frac{1}{N_B} \int_B d(\Delta\theta) d(\Delta\omega) t_k^{\text{node}}(\Delta\theta, \Delta\omega), \quad (15)$$

for an alternative characterisation of the nodes independent of the initial perturbation. Here, $N_{B_j} = \int_{B_j} d(\Delta\theta) d(\Delta\omega) = 8\pi^2 S_j$ and $N_B = \int_B d(\Delta\theta) d(\Delta\omega)$ are normalisation constants. Indeed, the times \bar{t}_j^{grid} and \bar{t}_j^{node} were found to approach constant values with increasing raster grid resolution and their values converged well for the resolution used.

Figures 8(a) and (b) show a comparison of the \bar{t}_j^{grid} and \bar{t}_j^{node} for the four model variants. In case of the homogenised grids, we find $\bar{t}_j^{\text{grid}} \simeq 3$ and $\bar{t}_j^{\text{node}} \simeq 2.5$ for all nodes. In the heterogeneous cases, by contrast, the \bar{t}_j^{grid} and \bar{t}_j^{node} vary strongly between different nodes and the times are in general significantly larger (with a few exceptions for the \bar{t}_j^{grid}).

As discussed above, perturbation of certain nodes in the heterogeneous models can lead to grid failure, and for the \bar{t}_j^{grid} it makes sense to distinguish between these BE nodes and the other ones. Therefore we have marked the BE nodes in figures 8(a) and (c) by full symbols. Let us remind that, according to equations (12) and (14), the times are determined with respect

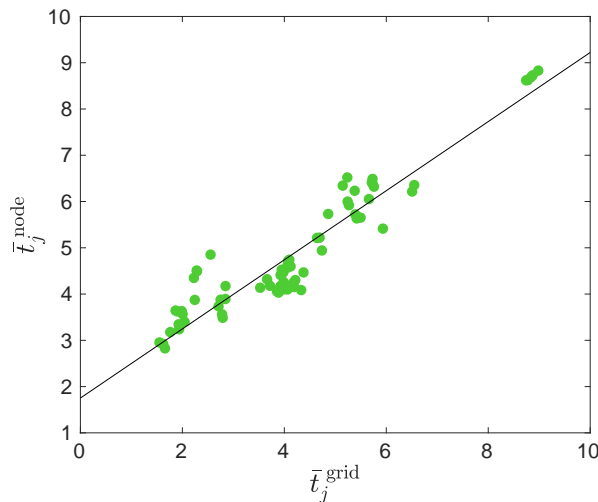


Figure 9. Scatter plot of the mean node return times \bar{t}_j^{node} versus the mean grid return times \bar{t}_j^{grid} for the model Het+IN. The line corresponds to a least square fit and the correlation coefficient is $R \cong 0.95$.

to the attraction basins \mathcal{B}_j , i.e. without including initial perturbations causing grid failure. As can be seen from figure 8(a), comparatively large \bar{t}_j^{grid} correspond to perturbations of the BE nodes.

A remarkable feature can be seen in the Het+IN model. For this model, the six particular large \bar{t}_j^{grid} in figure 8(a) are caused by perturbations of a node in the pairs (8, 9), (19, 20), and (30, 31). The nodes of these pairs are directly connected by a transmission line, see figure 1. Revisiting figure 4, we see that the grid failure probabilities of them are not large. Thus, in the Het+IN model we find nodes that rarely lead to grid failure but to long grid return times. Inspection of the environment of the respective node pairs in figure 1 reveals a characteristic pattern: One of the nodes of each pair (nodes 8, 19, and 30) is strongly coupled to a (load) node with small $|P_j^{(m)}|$ (and hence small H_j , see figure 3), and it has an appreciable additional coupling only to its pair partner. The latter can have several links to other nodes, but the coupling to its partner node is the dominant one. Accordingly, a perturbation of it becomes predominantly mediated to its partner.

Looking at the range of the \bar{t}_j^{grid} in figure 8(a), we obtain a slightly wider range from 1.5 to 9 for the Het+IN model compared to the range from 2.5 to 7 for the Het-IN variant. This shrinking of the range when neglecting internal nodes is even stronger for the \bar{t}_j^{node} , where we find a range from 3 to 9 for the Het+IN model and from 4 to 6.5 for the Het-IN variant, see figure 8(b). While there is no one-to-one correspondence with respect to the rank order of the return times \bar{t}_j^{grid} for the Het-IN and Het+IN model, large times \bar{t}_j^{grid} in the Het-IN model tend to be large also in the Het+IN model. A weak linear correlation is demonstrated in figure 8(c), with a (Pearson) correlation coefficient of $R \cong 0.85$. In contrast, almost no correlation ($R \cong 0.56$) between the node return times of the Het+IN and Het-IN models is found, see figure 8(d).

Finally, we analyse whether more disturbing nodes for the grid are also more susceptible for getting disturbed. Indeed, a scatter plot of \bar{t}_j^{grid} versus \bar{t}_j^{node} reveals a linear correlation

in the Het+IN model, see figure 9. The corresponding correlation coefficient is $R \cong 0.95$. Surprisingly, this feature is not seen in the Het-IN model. A linear correlation between \bar{t}_j^{grid} and \bar{t}_j^{node} is also seen in the homogenised models, but not of relevance in view the small variations of these times.

5. Summary and conclusions

For investigating the stability of power grids against single-node perturbations we have performed extensive numerical calculations for the IEEE RTS-96 grid. These were carried out for perturbations of the frequencies and voltage phase angles using the non-linear swing equations, as well as a treatment of generators and loads based on a synchronous machine approach. Four model variants were studied to analyse impacts of simplifications, which we referred to as Hom±IN and Het±IN according to homogenising grid properties and/or neglecting reactances between terminal and internal nodes. The stability of the grid after a perturbations was quantified by the probabilities of return to the fixed point state of synchronous operation (basin stability) and additionally by the times needed for return to this state. These return times allow for a characterisation of the nodes within the attraction basin of the fixed point, and they include also a measure for the susceptibility of a node towards a perturbation at another node. We introduced grid return times for specifying the perturbation strengths of nodes and node return times for specifying the susceptibility of nodes against perturbations.

The main results for the basin stability can be summarised as follows. When homogenising node and transmission line properties, the grid always returns to its synchronous state. This robustness occurs despite of the large perturbation region considered, which covers all possible voltage phase angles and frequency deviations of up to 1 Hz. In the heterogeneous models, perturbation of a couple of nodes can turn the system into a stationary state of grid failure with an asynchronous voltage phase dynamics. When taking into account the internal nodes, the overall grid stability increases. This may be expected from the effectively fully connected grid structure in this case, which should result in a more mean-field like behaviour with a weakening of heterogeneities.

Most perturbative nodes with highest probabilities of causing grid failure are different in the Het-IN and Het+IN model. In the Het-IN variant, these nodes can be correlated with topological features, namely they are part of dead ends. This feature has been earlier reported in [14] for a grid structure resembling the Hom-IN model, if allowing for extremely large frequency perturbations. For frequency perturbations of up to 1 Hz considered in this work, the correlation is seen only in the Het-IN model but not in the corresponding Hom-IN variant. Our results for the basin stability furthermore suggest that nodes being part of effective dead ends exhibit a large probability of causing grid failure when perturbed. The effective dead ends are associated with nodes of high inertia and accordingly slow response. In the Het+IN model, we found the mechanical power to be the dominant factor controlling basin stability.

Our results for the return times show that the largest times are about five seconds for the homogenised models. This is small compared to times scales of secondary control measures

starting at ten seconds [19, 26]. In contrast, return times for the heterogeneous models can be 20 seconds and larger. While grid and node return times in the homogenised models are almost the same for all nodes, a large spread is seen between different nodes in both the Het-IN and Het+IN models. This spread turned out to be slightly larger in the Het+IN compared to the Het-IN model, which is a bit surprising in view of the overall higher basin stability of the Het+IN model. In the Het+IN model a linear correlation between grid and node return times is found, meaning that nodes with higher perturbative capability have higher perturbation receptiveness also. This feature is not seen in the Het-IN variant.

We conclude that by homogenising node and transmission line properties in a power grid, while keeping its link topology, leads to a strong overestimation of grid stability. A neglect of reactances between points of power generation/consumption and points of power injection/ejection can cause wrong identification of most perturbing nodes in the grid and an underestimation of grid stability. It moreover influences the spread of return times as well as correlations between them.

Acknowledgments

We thank O. Kamps, J. Peinke, and K. Schmietendorf for very valuable discussions and gratefully acknowledge funding by the Deutsche Forschungsgemeinschaft (MA 1636/9-1).

References

- [1] Backhaus S and Chertkov M 2013 *Phys. Today* **66** 42–48
- [2] Timme M, Kocarev L and Witthaut D 2015 *New J. Phys.* **17** 110201
- [3] Auer S, Kleis K, Schultz P, Kurths J and Hellmann F 2016 *Eur. Phys. J. Spec. Top.* **225** 609–625
- [4] Mureddu M, Caldarelli G, Damiano A and Meyer-Ortmanns H 2016 *Sci. Rep.* **6** 34797
- [5] Schiel C, Lind P G and Maass P 2017 *Sci. Rep.* **7** 11562
- [6] Hähne H, Schottler J, Wächter M, Peinke J and Kamps O 2018 *EPL* **121** 30001
- [7] Tamrakar S, Conrath M and Kettemann S 2018 *Sci. Rep.* **8** 6459
- [8] Schäfer B, Beck C, Aihara K, Witthaut D and Timme M 2018 *Nat. Energy* **3** 119–126
- [9] Nishikawa T and Motter A 2015 *New J. Phys.* **17** 015012
- [10] Schmietendorf K, Peinke J, Friedrich R and Kamps O 2014 *Eur. Phys. J. Spec. Top.* **223** 2577–2592
- [11] Schmietendorf K, Peinke J and Kamps O 2017 *Eur. Phys. J. B* **90** 222
- [12] Filatrella, G, Nielsen, A H and Pedersen, N F 2008 *Eur. Phys. J. B* **61** 485–491
- [13] Lozano, S, Buzna, L and Díaz-Guilera, A 2012 *Eur. Phys. J. B* **85** 231–238
- [14] Menck P, Heitzig J, Kurths J and Schellnhuber H 2014 *Nat. Commun.* **5** 3969
- [15] Grigg C, Wong P, Albrecht P, Allan R, Bhavaraju M, Billinton R, Chen Q, Fong C, Haddad S, Kuruganty S and et al 1999 *IEEE Trans. Pow. Sys.* **14** 1010–1020
- [16] Li C, Sun Y and Chen X 2007 Analysis of the blackout in Europe on November 4, 2006, 2007 *International Power Engineering Conference – IPEC 2007* (IEEE, New Jersey) pp 939–944
- [17] Menck P J, Heitzig J, Marwan N and Kurths J 2013 *Nat. Phys.* **9** 89–92
- [18] Mitra C, Kittel T, Choudhary A, Kurths J and Donner R V 2017 *New J. Phys.* **19** 103004
- [19] Machowski J, Bialek J and Bumby J 2008 *Power System Dynamics* (John Wiley & Sons, New Jersey)
- [20] Zimmerman R and Murillo-Sánchez C 2016 *Matpower 6.0b1 User Manual* (Online, Power Systems Engineering Research Center (PSerc), available at www.pserc.cornell.edu/matpower/manual.pdf)
- [21] Doerfler F and Bullo F 2013 *IEEE Trans. Circuits Syst. I Regul. Pap.* **60** 150–163

- [22] Kuramoto Y 1975 Self-entrainment of a population of coupled non-linear oscillators *Mathematical Problems in Theoretical Physics (Lecture Notes in Physics vol 39)* ed Araki H (Springer Verlag, Berlin) pp 420–422
- [23] Acebrón J A, Bonilla L L, Pérez Vicente C J, Ritort F and Spigler R 2005 *Rev. Mod. Phys.* **77** 137–185
- [24] Rodrigues F A, Peron T K D, Ji P and Kurths J 2016 *Phys. Rep.* **610** 1–98
- [25] Rohden M, Sorge A, Timme M and Witthaut D 2012 *Phys. Rev. Lett.* **109** 064101
- [26] 2004 UCTE operation handbook. Available at <https://www.entsoe.eu>
- [27] Mehta D, Daleo N, Dörfler F and Hauenstein J 2015 *Chaos* **25** 053103
- [28] Delabays R, Coletta T and Jacquod P 2016 *J. Math. Phys.* **57** 032701
- [29] Motter A, Myers S, Anghel M and Nishikawa T 2012 *Nat. Phys.* **9** 191–197
- [30] Witthaut D and Timme M 2012 *New J. Phys.* **14** 083036
- [31] Jung D and Kettemann S 2016 *Phys. Rev. E* **94** 012307